

# Parallel and Scalable Heat Method

JIONG TAO, University of Science and Technology of China  
 JUYONG ZHANG\*, University of Science and Technology of China  
 BAILIN DENG, Cardiff University  
 ZHENG FANG, Nanyang Technological University  
 YUE PENG, University of Science and Technology of China  
 YING HE, Nanyang Technological University

The heat method is a popular approach to computing geodesic distances on discrete domains. It first performs short-time heat diffusion to approximate the gradient direction of the geodesic distance function, followed by least-squares recovery of the actual distance. It only requires solving two sparse linear systems, which can be done efficiently using matrix prefactorization. However, it does not scale well to large models, due to the large memory consumption for matrix factorization and the difficulty in its parallelization. In this paper, we propose an improved version of the heat method which overcomes its limitation in scalability. Our key observation is that the recovery of geodesic distance from approximate gradient directions can be reformulated as gradient optimization problem that enforces integrability, which can be solved using a parallel fixed-order method that requires no linear system solving and converges quickly. Afterwards, the geodesic distance are efficiently recovered by parallel integration of the optimized gradients in breadth-first order. Moreover, a similar breadth-first strategy is developed for a parallel Gauss-Seidel solver for heat diffusion. Our approach is trivially parallelizable, with a low memory footprint that grows linearly with respect to the model size. This makes it particularly suitable for handling large models. Experimental results show that our method can efficiently compute geodesic distance on meshes with up to 99 million vertices on a desktop PC with 128GB RAM, outperforming the original heat method and other state-of-the-art geodesic distance solvers.

CCS Concepts: •Theory of computation → Computational geometry; Convex optimization;

Additional Key Words and Phrases: Heat method, scalability, parallel algorithm, heat diffusion, linear time complexity

## ACM Reference format:

Jiong Tao, Juyong Zhang, Bailin Deng, Zheng Fang, Yue Peng, and Ying He. 2016. Parallel and Scalable Heat Method. 1, 1, Article 1 (January 2016), 9 pages.  
 DOI: 10.1145/nnnnnnn.nnnnnnn

## 1 INTRODUCTION

The heat method (HM) [Crane et al. 2013, 2017] is a popular approach to computing geodesic distances on discrete domains, such as regular grids, point clouds, triangle meshes, and tetrahedral meshes. It is based on Varadhan’s formula [Varadhan 1967] that relates the heat kernel and geodesic distance:

$$\lim_{t \rightarrow 0} -4t \log h(t, x, y) = d^2(x, y),$$

\*Corresponding author (juyong@ustc.edu.cn).

© 2016 ACM. This is the author’s version of the work. It is posted here for your personal use. Not for redistribution. The definitive Version of Record was published in, <http://dx.doi.org/10.1145/nnnnnnn.nnnnnnn>.

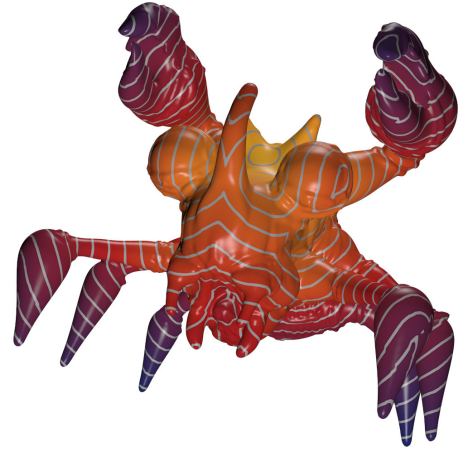


Fig. 1. Our method has linear time and space complexities and scales well. It takes 2912.05 seconds under eight threads on the Thundercrab model with 99 million vertices on a PC with 128 GB memory and a octa-core CPU at 3.6 GHz. The state-of-the-art exact method VTP [Qin et al. 2016] takes 22271.69 seconds, and the heat method [Crane et al. 2013] runs out of memory.

where  $x, y$  are arbitrary pair of points on a Riemannian manifold  $M$ ,  $t$  is the diffusion time,  $h(t, x, y)$  and  $d(x, y)$  are the heat kernel and geodesic distance respectively. The heat method is conceptually simple and elegant. Since the geodesic distance is a solution to the eikonal equation

$$\|\nabla d\| = 1, \quad (1)$$

the heat method first integrates the heat flow  $\dot{u} = \Delta u$  for a short time and normalizes its gradient to derive a unit vector field  $\mathbf{H}$  that approximates the geodesic distance gradient. Afterwards, it determines the geodesic distance by finding scalar field  $d$  whose gradient is the closest to  $\mathbf{H}$ , which simply amounts to solving a Poisson system. The heat method involves only sparse linear systems, which can be pre-factorized once and reused to solve different right-hand-sides in linear time. This feature makes it highly attractive for applications where geodesic distances are required repeatedly. However, the Cholesky factorization used in [Crane et al. 2013, 2017] requires a substantial amount of computational time and memory for large meshes. As a result, the heat method does not scale well. Although we can replace the Cholesky direct solver with iterative solvers with lower memory consumption such as the Krylov space methods, these solvers can still take a larger number of iterations with long computational time.

The goal of this work is to develop a scalable algorithm for computing geodesic distance on mesh surfaces. Our method follows a similar approach as the heat method, first computing approximate gradients via heat diffusion and then using them to recover the distance. Our main insight is that instead of solving the Poisson system, we can perform the second step indirectly with much better efficiency and scalability. Specifically, we first compute the an integrable gradient field that the closest to the unit vector field derived from heat diffusion, then integrate this field to obtain the geodesic distance. Computing the gradient field is a convex optimization problem, which can be solved efficiently using alternating direction method of multiplies (ADMM) [Boyd et al. 2011], a first-order method with fast convergence. Unlike previous ADMM solvers that optimize function variables to regularize the gradients, our formulation uses gradient as variables, such that each step of the solver only involves a separable subproblem and is trivially parallelizable. The resulting gradient field can be efficiently integrated using a parallel Gauss-Seidel solver, which is more efficient and robust for large meshes than direct and iterative linear solvers. The resulting method is both efficient and scalable, and can be run in parallel on multi-core processors to gain significant speedup. We evaluate the performance of our method using a variety of mesh models in different sizes. Our method significantly outperforms the original heat method while achieve similar accuracy. Moreover, the computational time and memory consumption of our approach grows linearly with the mesh size, allowing to handle much larger meshes than the heat method.

### 1.1 Our Contributions

Our main contribution is a new method that computes geodesic distance on mesh surfaces in an efficient and scalable way, which includes:

- A parallel Gauss-Seidel solver for solving short-time heat diffusion from source vertices, which is more scalable and numerically more robust than directly solving the heat diffusion linear system in [Crane et al. 2013].
- A convex optimization formulation for correcting the unit vector field derived from heat diffusion into an integrable gradient field, and an ADMM solver for solving the problem. Our solver is trivially parallelizable, and has linear time and space complexity.
- An efficient parallel integration scheme to recover geodesic distance from the gradient field.

## 2 RELATED WORK

Computing geodesic distances on discrete domains has been studied extensively in the past 3 decades. There are two major classes of algorithms, which are based on computational geometry and partial differential equation (PDE), respectively.

Computational geometry approaches [Chen and Han 1990; Mitchell et al. 1987] maintain wavefront on mesh edges and propagate it across the faces in a Dijkstra-like sweep. They work for arbitrary manifold triangle meshes and can compute exact polyhedral distances. However, they are too computationally expensive to apply for time-critical applications. Although acceleration schemes are

---

### ALGORITHM 1: The Parallel and Scalable Heat Method

---

**Data:**  $\mathcal{M} = (\mathcal{V}, \mathcal{E}, \mathcal{F})$ : a manifold triangle mesh;  $v_s$ : the source vertex;  $t$ : heat diffusion time;  $D_{\max}$ : maximum iterations of heat diffusion.

**Result:** The geodesic distances  $d_i$  for each vertex  $v_i, i \in \mathcal{V}$ .

```

// Heat diffusion from source vertex
1  $\{u_i, i \in \mathcal{V}\} = \text{Diffusion}(\mathcal{M}, v_s, t)$ ;
// Gradient normalization
2  $\mathbf{H} = -\frac{\nabla u}{\|\nabla u\|}$ ;
// Compute integrable gradient field
3  $\mathbf{G} = \text{Integrable}(\mathcal{M}, \mathbf{H})$ ;
// Recover geodesic distance
4  $\{d_i, i \in \mathcal{V}\} = \text{Recovery}(\mathcal{M}, v_s, \mathbf{G})$ ;

```

---

available [Qin et al. 2016; Surazhsky et al. 2005; Xin and Wang 2009; Ying et al. 2013, 2014], they are difficult to implement, and cannot adapt to discrete domains other than triangle meshes.

PDE methods are much more efficient and flexible. The fast marching method (FMM) [Kimmel and Sethian 1998] directly solves the Eikonal equation by iteratively building the solution outward from the points with known/smallest distance values on regular grids and triangulated surfaces. It runs in an optimal  $O(n \log n)$  time on a triangle mesh with  $n$  vertices. Weber et al. [2008] developed a highly efficient parallel FMM on geometry images, which runs in  $O(n)$  time. The heat method, proposed by Crane et al. [2013], adopts a different strategy. Rather than solving the distances directly, it first computes a unit vector field that approximates the gradient of the geodesic distances, then integrates the gradient by solving a Poisson equation. Based on this novel strategy, heat method only needs to solve two linear systems. Belyaev and Fayolle [2015] extended the normalization-integration idea to compute the general  $L_p$  distance to a 2D curve or 3D surface, and they solve the optimization problem via ADMM.

The saddle vertex graph method [Ying et al. 2013] is a completely different approach. It first computes a sparse undirected graph  $G$ , whose edges are direct geodesic paths (which cannot be partitioned into smaller segments). Then computing single- or multi-sources geodesic distances is equivalent to find shortest paths on  $G$ , which can be solved using Dijkstra's algorithm. Constructing the graph takes  $O(nK^2 \log K)$  time and computing geodesic distances takes  $O(Kn \log n)$  time, where  $K$  is the maximal degree. As a pre-computation method, SVG is efficient and the saddle vertex graph can be constructed in parallel. However, computing the distances is intrinsically sequential. Our method does not require pre-computation, and all its three steps can be implemented in parallel.

## 3 ALGORITHM

Given a triangle mesh  $\mathcal{M} = (\mathcal{V}, \mathcal{E}, \mathcal{F})$  and a source vertex  $v_s$ , we want to compute the geodesic distance  $d_i$  from each vertex  $v_i$  to  $v_s$  by solving the eikonal equation with boundary condition  $d(v_s) = 0$ . The *direct* solver (e.g., the fast marching method [Kimmel and Sethian 1998]) does not scale well due to its  $O(n \log n)$  time complexity. Inspired by the heat method [Crane et al. 2013, 2017], we develop a gradient-based *indirect* solver for the eikonal equation.

Similar to the heat method, we first construct a unit vector  $\{\mathbf{h}_i\}$  for each face  $f_i$  using short-time heat diffusion from the source vertex. Such a vector field provides good approximation to the gradient field of the geodesic distance function, but is in general not integrable. The geodesic distance is then computed as a scalar field whose gradient is as close to  $\mathbf{h}_i$  as possible. Different from the original heat method that computes heat diffusion and recovers geodesic distance by directly solving linear systems, we perform these steps using iterative methods: heat diffusion is done via Gauss-Seidel iteration, while the geodesic distance is computed by first correcting  $\{\mathbf{h}_i\}$  into an integrable field  $\{\mathbf{g}_i\}$  and then integrating it from the source vertex. Algorithm 1 shows the pipeline of our method, and Fig. 2 shows the algorithm process on bunny model. The main benefit of our approach is its scalability: both the Gauss-Seidel heat diffusion and the geodesic distance integration can be done in parallel through breadth-first traversal over the mesh surface; the correction of  $\{\mathbf{h}_i\}$  is a simple convex optimization problem and computed using an ADMM solver where each step is trivially parallelizable. Moreover, both the Gauss-Seidel solver and the ADMM solver converge quickly to a solution with reasonable accuracy, resulting in much less computational time than the original heat method. Moreover, our approach has a low memory footprint that grows linearly with mesh size, allowing it to handle very large meshes while the original heat method fails on such models due to the memory consumption of matrix factorization.

To facilitate the presentation of our method, we assume in this section that  $M$  is a topological disk and there is only one source vertex. More general cases, such as meshes with arbitrary topology and multiple source vertices, will be discussed in Section 4.

### 3.1 Heat Diffusion

Following [Crane et al. 2013, 2017], we compute the initial vector field  $\{\mathbf{h}_i\}$  by integrating the heat flow  $\dot{u} = \Delta u$  of a scalar field  $u$  for a short time  $t$ , and taking

$$\mathbf{h}_i = -\frac{\nabla u|_{f_i}}{\|\nabla u|_{f_i}\|}. \quad (2)$$

The initial value of the scalar field  $u$  is a Dirac delta function for a source vertex. Integrating the heat flow using a single backward Euler step leads to a linear system [Crane et al. 2013, 2017]:

$$(\mathbf{A} - t\mathbf{L}_c)\mathbf{u} = \mathbf{u}_0, \quad (3)$$

where vector  $\mathbf{u}$  stores the value of  $u$  for each vertex, vector  $\mathbf{u}_0$  has value 1 for the source vertex and 0 for all other vertices,  $\mathbf{A}$  is a diagonal matrix storing the area of each vertex, and  $\mathbf{L}_c$  is the cotan Laplacian matrix. Crane et al. [2013; 2017] solved this sparse linear system by prefactorizing matrix  $\mathbf{A} - t\mathbf{L}$  using Cholesky decomposition. This approach works well for meshes with up to a few million vertices, but faces difficulties for larger meshes due to high memory consumption for the factorization. Alternatively, we can solve the system using Krylov subspace methods such as conjugate gradient (CG), which requires less memory and can be parallelized [Greenbaum et al. 1989]. However, CG may require a large number of iterations to converge for large meshes, which still results in significant computational costs.

With scalability in mind, we prefer a method that can be run in parallel, without requiring many iterations to converge. Therefore, we solve the system (2) with Gauss-Seidel iteration in breadth-first order, where all vertices with the same topological distance to the source are updated in parallel. Specifically, let us define the sets

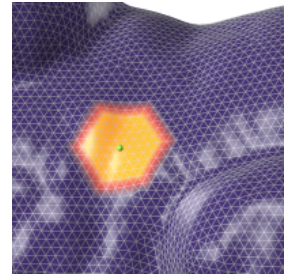
$$\begin{aligned} \mathcal{D}_0 &:= \{v_s\}, \\ \mathcal{D}_1 &:= \mathcal{N}(\mathcal{D}_0) \setminus \mathcal{D}_0, \\ \mathcal{D}_2 &:= \mathcal{N}(\mathcal{D}_1) \setminus (\mathcal{D}_0 \cup \mathcal{D}_1), \\ &\dots \\ \mathcal{D}_i &:= \mathcal{N}(\mathcal{D}_{i-1}) \setminus \bigcup_{k=0}^{i-1} \mathcal{D}_k, \end{aligned} \quad (4)$$

where  $\mathcal{N}(\cdot)$  denotes the union of one-ring neighbor vertices. Intuitively,  $\mathcal{D}_i$  is the set of vertices that require at least  $i$  hops from the source  $v_s$  to reach. All such sets can be determined using breadth-first traversal of the vertices starting from  $v_s$ . Then in each outer iteration of our Gauss-Seidel solver, we update the values at vertex sets  $\mathcal{D}_0, \mathcal{D}_1, \dots$  consecutively. When updating a set  $\mathcal{D}_i$ , we determine the new values for each vertex  $v_j$  from the latest values of its neighboring vertices to satisfy its corresponding equation in (3), resulting in an update rule

$$u^i(v_j) = \frac{u_0(v_j) + t \sum_{k \in \mathcal{N}_j} \theta_{j,k} u^{i-1}(v_k)}{A_j + t \sum_{k \in \mathcal{N}(j)} \theta_{j,k}}, \quad (5)$$

where  $A_v$  is the area for vertex  $v$ ,  $\mathcal{N}_j$  denotes the index set of neighboring vertices for  $v_j$ ,  $u_0(v_j)$  is the initial value of  $v_j$ ,  $u^{i-1}(v_k)$  is the value at  $v_k$  after the update of  $\mathcal{D}_{i-1}$ , and  $\theta_{j,k}$  is the coefficient of  $v_k$  for the cotan Laplacian at  $v_j$ . Intuitively, each outer iteration sweeps all vertices in breadth-first order starting from the source, where all vertices at the current front are updated simultaneously using the latest values. Note that unless it is close to the source, the set  $\mathcal{D}_i$  often contains a large number of vertices. Thus the update can be easily parallelized with little overhead. In our experiments, the solver quickly converges to a solution that is good enough for the subsequent steps. An illustration figure of our heat diffusion method is shown in the inset. The green point is the source vertex, which diffuses the heat from near to far area. In current state, the vertices in the yellow part are already processed, and the heat value of vertices in the red part are being updated in parallel. For the Sphere model in Fig. 3 with 163842 vertices, it separately takes 256 and 326 iterations to produce a result with 1% and 0.1% average error with the solution by directly solving Eq. (3), significantly reducing the computational time compared with the direct solver and the Krylov subspace method. The mean error  $E$  is computed based on the following equation:

$$E = \sqrt{\sum_{i=1}^{|\mathcal{F}|} A_i \|h_i - h_i^*\|^2}, \quad (6)$$



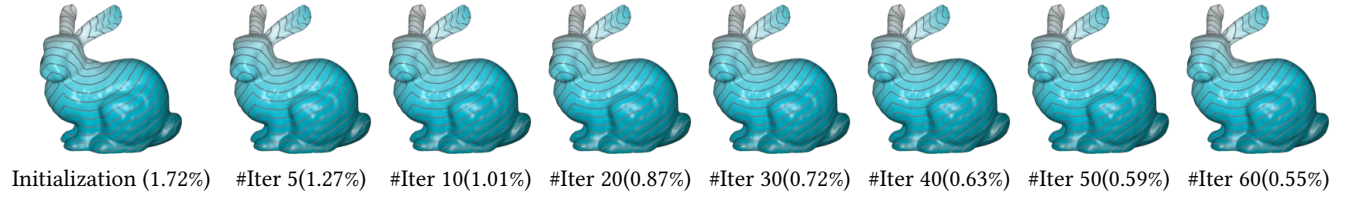


Fig. 2. Illustration the algorithm pipeline of our method. The first one shows the geodesic distance by integration the initial gradient  $\{\mathbf{h}_i\}$  via the method in Section 3.1. The remaining shows the geodesic distance of the intermediate  $\{\mathbf{g}_i\}$  computed in Section 3.2. The geodesic distance is recovered from gradient by the method in Section 3.3. The value in the bracket is the relative error with heat method [Crane et al. 2013].

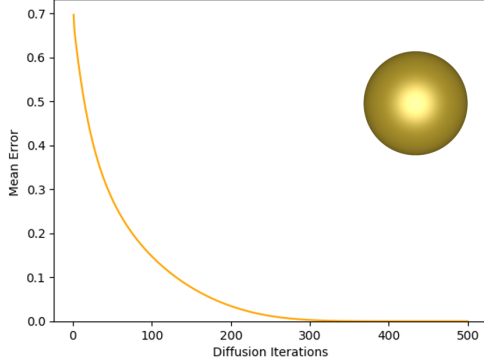


Fig. 3. This figure shows how the mean error changes along with the number of diffusion iterations. The mean error is computed based on Eq. 6.

where  $A_i$  is the normalized area of face  $f_i$  with respect to the total surface area,  $h_i$  is the normalized face gradient by our method and  $h_i^*$  is the normalized face gradient by directly solving Eq. (3).

### 3.2 Integrable Gradient Field

In general, the unit vector field  $\{\mathbf{h}_i\}$  is not integrable. To derive geodesic distance, the heat method computes a scalar field whose gradients are as close as possible to  $\{\mathbf{h}_i\}$ , and shifts its values such that it becomes zero at the source vertex. This is achieved in [Crane et al. 2013, 2017] by solving a Poisson linear system

$$\mathbf{L}\mathbf{d} = \mathbf{b}, \quad (7)$$

where vector  $\mathbf{d}$  stores the values of the scalar field, and  $\mathbf{b}$  stores the integrated divergence of the field  $\{\mathbf{h}_i\}$  at the vertices. Similar to heat diffusion, solving this linear system using Cholesky decomposition or Krylov subspace methods will face scalability issues. Therefore, we adopt a different strategy to derive geodesic distance: we first compute an integrable gradient field  $\{\mathbf{g}_i\}$  that is the closest to  $\{\mathbf{h}_i\}$ , and then integrate it to recover the geodesic distance. In the following, we will show that both steps can be performed using efficient and scalable algorithms.

Representing both  $\{\mathbf{h}_i\}$  and  $\{\mathbf{g}_i\}$  as 3D vectors, we compute  $\{\mathbf{g}_i\}$  by solving a convex constrained optimization problem:

$$\min_{\{\mathbf{g}_i\}} \sum_{f_i \in \mathcal{F}} A_i \|\mathbf{g}_i - \mathbf{h}_i\|^2, \quad (8)$$

$$\text{s.t. } \bar{\mathbf{e}} \cdot (\mathbf{g}_1^e - \mathbf{g}_2^e) = 0, \quad \forall e \in \mathcal{E}_{\text{int}}, \quad (9)$$

where  $\mathcal{E}_{\text{int}}$  denotes the set of interior edges,  $\bar{\mathbf{e}} \in \mathbb{R}^3$  is the unit vector for edge  $e$ , and  $\mathbf{g}_1^e, \mathbf{g}_2^e$  are the gradient vectors on the two incident faces for  $e$ . The constraint (9) is a compatibility condition that the gradient vectors on any pair of adjacent faces to have the same projection on their common edge, thus ensuring the global integrability of the vector field  $\{\mathbf{g}_i\}$  on a zero-genus surface.

To solve this problem in a scalable way, we introduce for each interior edge a pair of auxiliary variables  $\mathbf{y}_1^e, \mathbf{y}_2^e \in \mathbb{R}^3$  for the gradients on its adjacent faces, and reformulate the problem as

$$\begin{aligned} \min_{\{\mathbf{g}_i\}, \{\mathbf{y}_1^e, \mathbf{y}_2^e\}} & \sum_{f_i \in \mathcal{F}} A_i \|\mathbf{g}_i - \mathbf{h}_i\|^2 + \sum_{e \in \mathcal{E}_{\text{int}}} \sigma_e(\mathbf{y}_1^e, \mathbf{y}_2^e) \quad (10) \\ \text{s.t.} & \text{ for each } f_i \in \mathcal{F} : \mathbf{g}_i = \mathbf{y}_k \quad \forall \mathbf{y}_k \in \mathcal{Y}_i. \quad (11) \end{aligned}$$

Here  $A_i$  is the face area for  $\mathbf{g}_i$ , and  $\sigma_e(\cdot)$  is an indicator function for compatibility between the auxiliary gradient variables on the two incident faces of edge  $e$ :

$$\sigma_e(\mathbf{y}_1^e, \mathbf{y}_2^e) = \begin{cases} 0, & \text{if } \bar{\mathbf{e}} \cdot (\mathbf{y}_1^e - \mathbf{y}_2^e) = 0, \\ +\infty, & \text{otherwise.} \end{cases} \quad (12)$$

$\mathcal{Y}_i$  denotes the set of auxiliary variables associated with face  $f_i$ , such that constraint (11) enforces consistency between the auxiliary variables and the actual gradient vectors. To facilitate presentation, we write it in matrix form as

$$\begin{aligned} \min_{\mathbf{G}, \mathbf{Y}} & \|\mathbf{M}(\mathbf{G} - \mathbf{H})\|_F^2 + \sigma(\mathbf{Y}), \quad (13) \\ \text{s.t.} & \mathbf{M}(\mathbf{Y} - \mathbf{S}\mathbf{G}) = \mathbf{0}. \end{aligned}$$

where  $\mathbf{G}, \mathbf{H} \in \mathbb{R}^{|\mathcal{F}| \times 3}$  and  $\mathbf{Y} \in \mathbb{R}^{2|\mathcal{E}_{\text{int}}| \times 3}$  collect the gradient variables, the input unit vector fields, and the auxiliary variables, respectively.  $\sigma(\mathbf{Y})$  denotes the sum of indicator functions for auxiliary variable pairs.  $\mathbf{S} \in \mathbb{R}^{2|\mathcal{E}_{\text{int}}| \times |\mathcal{F}|}$  is a selection matrix that chooses the matching gradient variable for each auxiliary variable.  $\mathbf{M} \in \mathbb{R}^{2|\mathcal{E}_{\text{int}}| \times 2|\mathcal{E}_{\text{int}}|}$  is a diagonal matrix storing the square roots of face areas associated with the auxiliary variables. Introducing  $\mathbf{M}$  in the constraints does not alter the solution, but helps to make the algorithm robust to the mesh discretization. Indeed, a similar constraint reweighting strategy is employed in [Overby et al. 2017] to improve the convergence of their ADMM solver for physics simulation.

To solve this problem, ADMM searches for a saddle point of its augmented Lagrangian

$$L(\mathbf{G}, \mathbf{Y}, \boldsymbol{\lambda}) = \|\mathbf{M}(\mathbf{G} - \mathbf{H})\|_F^2 + \sigma(\mathbf{Y}) + \text{tr}(\boldsymbol{\lambda}^T \mathbf{M}(\mathbf{Y} - \mathbf{S}\mathbf{G})) + \frac{\mu}{2} \|\mathbf{M}(\mathbf{Y} - \mathbf{S}\mathbf{G})\|_F^2$$

where  $\lambda \in \mathbb{R}^{2|\mathcal{E}_{\text{int}}| \times 3}$  collects the dual variables, and  $\mu > 0$  is a penalty parameter. The stationary point is computed iteratively, by alternating between the updates of  $Y$ ,  $G$ , and  $\lambda$ .

**Y-update.** This step minimizes the augmented Lagrangian with respect to  $Y$ , while fixing  $G$  and  $\lambda$ . It reduces to

$$\min_Y \sigma(Y) + \frac{\mu}{2} \left\| \mathbf{M}(Y - \text{SG}) + \frac{\lambda}{\mu} \right\|_F^2.$$

This is separable into a set of independent subproblems for each internal edge  $e$ :

$$\min_{y_1^e, y_2^e} \sigma_e(y_1^e, y_2^e) + \frac{\mu}{2} \left( \left\| \alpha_1^e (y_1^e - \mathbf{g}_1^e) + \frac{\lambda_1^e}{\mu} \right\|^2 + \left\| \alpha_2^e (y_2^e - \mathbf{g}_2^e) + \frac{\lambda_2^e}{\mu} \right\|^2 \right),$$

where  $\alpha_i^e$ ,  $\mathbf{g}_i^e$ ,  $\lambda_i^e$  ( $i = 1, 2$ ) are the face area square root, gradient variables, and dual variables corresponding to  $y_i^e$ , respectively. This problem has a closed-form solution

$$\begin{aligned} y_1^e &= \mathbf{q}_1^e + \frac{A_2^e}{A_1^e + A_2^e} \bar{\mathbf{e}} \cdot (\bar{\mathbf{e}} \cdot (\mathbf{q}_2^e - \mathbf{q}_1^e)), \\ y_2^e &= \mathbf{q}_2^e - \frac{A_1^e}{A_1^e + A_2^e} \bar{\mathbf{e}} \cdot (\bar{\mathbf{e}} \cdot (\mathbf{q}_2^e - \mathbf{q}_1^e)), \end{aligned}$$

where  $\mathbf{q}_i^e = \mathbf{g}_i^e - \frac{\lambda_i^e}{\mu \alpha_i^e}$ , and  $A_i^e$  is the face area for  $y_i^e$ , for  $i = 1, 2$ .

**G-update.** After updating  $Y$ , we fix  $Y$ ,  $\lambda$  and minimize the augmented Lagrangian with respect to  $G$ , which reduces to independent subproblems

$$\min_{\mathbf{g}_i} A_i \|\mathbf{g}_i - \mathbf{h}_i\|^2 + \frac{\mu}{2} \sum_{y_k \in \mathcal{Y}(i)} \left\| \alpha_i (y_k - \mathbf{g}_i) + \frac{\lambda_k}{\mu} \right\|^2, \quad (14)$$

where  $\mathcal{Y}(i)$  denotes the set of associated auxiliary variables for  $\mathbf{g}_i$  in  $Y$ , and  $\lambda_k$  denotes the corresponding components in  $\lambda$  for  $y_k$ . These subproblems can be solved in parallel with closed-form solution

$$\mathbf{g}_i = \frac{2\mathbf{h}_i + \mu \sum_{y_k \in \mathcal{Y}(i)} (y_k + \frac{\lambda_k}{\mu \alpha_i})}{2 + \mu |\mathcal{Y}(i)|}.$$

**$\lambda$ -update.** After the updates for  $Y$  and  $G$ , we update the dual variables  $\lambda$  as

$$\lambda = \lambda + \mu \mathbf{M}(Y - \text{SG}).$$

**Convergence.** Since the optimization problem (13) is convex, ADMM converges to a stationary point of the problem [Boyd et al. 2011]. We measure the convergence using the primal  $\mathbf{r}_{\text{primal}}$  and the dual residual  $\mathbf{r}_{\text{dual}}$  [Boyd et al. 2011]:

$$\mathbf{r}_{\text{primal}} = \mathbf{M}(Y - \text{SG}), \quad \mathbf{r}_{\text{dual}} = \mu \mathbf{A} \mathbf{S} \delta \mathbf{G},$$

where  $\delta \mathbf{G}$  is the difference of  $G$  between two iterations. We terminate the algorithm when both of the primal residual and dual residual are small enough, or the iteration count exceeds a user-specified threshold  $I_{\text{max}}$ . The residual thresholds are set to  $\|\mathbf{r}_{\text{primal}}\| \leq \|\mathbf{M}\|_F \cdot \epsilon_1$  and  $\|\mathbf{r}_{\text{dual}}\| \leq \|\mathbf{M}\|_F \cdot \epsilon_1$ .

The main advantage of using ADMM is that it quickly converges to a point close to the final solution [Boyd et al. 2011]. In the test examples, our algorithm only needs a small number of iterations to achieve a small primal residual and dual residual, and the Sphere example is shown in Fig. 4. Moreover, the updates of  $Y$ ,  $G$ , and

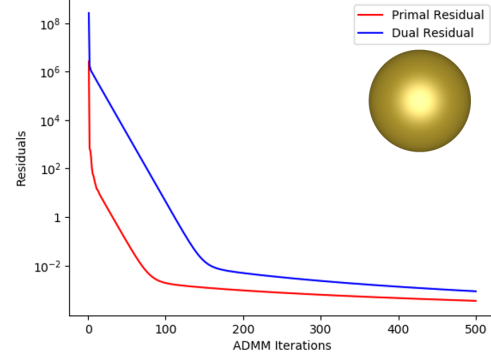


Fig. 4. This figure shows how the primal residual and dual residual change along with the number of ADMM iterations.

$\lambda$  are all trivially parallelizable, allowing for significant speedup on multi-core processors. Finally, the memory consumption grows linearly with the mesh size, making it feasible to process very large meshes. As a result, our method is both efficient and scalable.

*Remark.* Our formulation using gradients as variables is a key factor in achieving efficiency and scalability for the ADMM solver. In the past, ADMM and other first-order methods have been used to solve various optimization problems that involve regularization of gradients for certain functions [Heide et al. 2016; Ng et al. 2010; Wang et al. 2008; Xu et al. 2011]. These optimization problems are all formulated with the function values as the variables. For such problems, the solver typically includes a local step that updates auxiliary gradient variables according to the regularization, and a global step that updates the function variables to align with the auxiliary gradients. The global step requires solving a linear system for all the function variables, which will eventually become the bottleneck for large-scale problems. By formulating the problem using gradient variables instead, the global step of our solver reduces to a simple weighted averaging of a few auxiliary gradients, which is separable between different faces and can be done in parallel. From another perspective, the global step for a gradient optimization problem using function variables integrates the auxiliary gradients, which is globally coupled and limits parallelism. By using gradient variables, we bypass the more time-consuming global integration step, and postpone it to a later stage where we recover geodesic distance from the resulting integrable gradient field.

### 3.3 Integration

After computing an integrable gradient field  $\mathbf{g}_i$ , we determine the geodesic distance  $d$  at each vertex by setting  $d(v_s) = 0$  and integrating  $\mathbf{g}_i$  starting from the source  $v_s$ . Similar to the heat diffusion process, we determine the geodesic distance in breadth-first order, processing the vertex sets  $\mathcal{D}_1, \mathcal{D}_2, \dots$  consecutively. For a vertex  $v_j \in \mathcal{D}_i$  ( $i \geq 0$ ), its geodesic distance is determined from a neighboring vertex  $v_k \in \mathcal{D}_{i-1}$  via

$$d(v_j) = d(v_k) + \frac{1}{|\mathcal{T}_{jk}|} \sum_{f_l \in \mathcal{T}_{jk}} \mathbf{g}_l \cdot (\mathbf{p}_j - \mathbf{p}_k), \quad (15)$$

where  $\mathbf{p}_j, \mathbf{p}_k \in \mathbb{R}^3$  are the positions of  $v_j, v_k$ , and  $\mathcal{T}_{jk}$  denotes the set of faces that contain both  $v_j$  and  $v_k$ . The pairing between  $v_j$  and  $v_k$  can be determined using breadth-first traversal from the source vertex. In our implementation, we pre-compute the vertex sets  $\{\mathcal{D}_i\}$  as well as the vertex pairing using one run of breadth-first traversal, and reuse the information in the heat diffusion and geodesic distance integration steps. Just like our heat diffusion solver, the integration step (15) is independent between the different vertices within  $\mathcal{D}_i$ , thus can be performed in parallel with little overhead.

## 4 EXTENSIONS

Algorithm 1 is limited to genus-zero surfaces with a single source vertex. In this section, we extend it to meshes with arbitrary topology and multiple sources.

### 4.1 Complex Topology

On a surface with genus zero, the compatibility condition (9) ensures the gradient field is globally integrable. This is no longer true for other topologies. One example is shown in the inset. For a cylindrical mesh we can construct a unit vector field that is consistently oriented along the directrix and satisfies the compatibility condition (9). This vector field is not the gradient field of a scalar function, however, because integrating along a directrix will result in a different value when coming back to the starting point. In general, for a tangent vector field on a surface of arbitrary topology to be a gradient field, we must ensure its line integral along any closed curve vanishes. On a mesh surface of genus  $g$ , such a closed curve can be generated from a cycle basis that consists of  $2g$  independent non-contractible cycles [Crane et al. 2010]. Therefore, in addition to the compatibility condition (9), we enforce an integrability condition of the field  $\{\mathbf{g}_i\}$  on each cycle in the basis.

Similar to [Crane et al. 2010], we first compute a cycle basis for the dual graph of the mesh, using the tree-cotree decomposition of Eppstein [2003]. Each cycle is a closed loop  $C$  of faces. Connecting the mid-points of edges that correspond to the dual edges on  $C$ , we obtain a close polyline  $P$  lying on the mesh surface, with each segment lying on one face of the loop (see inset). Then the integrability condition on this cycle can be written as

$$\sum_{f_i \in C} \mathbf{g}_i \cdot \mathbf{v}_i^P = 0, \quad (16)$$

where  $C$  denotes the set of faces on the cycle, and  $\mathbf{v}_i^P \in \mathbb{R}^3$  is the vector of polyline segment on face  $f_i$ . Adding these conditions to the optimization problem (8)-(9), we derive a new formulation that finds a globally integrable gradient field closest to  $\{\mathbf{h}_i\}$ . This new problem is still convex, and can be solved similarly using ADMM.

Fig. 5 shows examples of geodesic distance on non-zero genus surfaces computed using the new formulation. The addition of

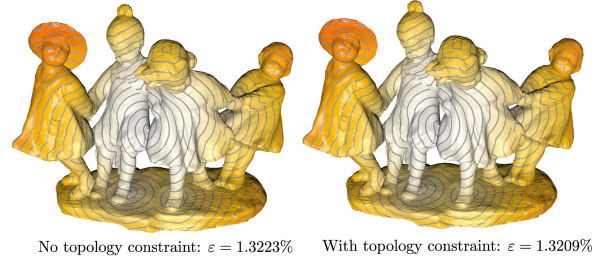


Fig. 5. Geodesic distance on a surface of genus eight, computed with and without the topological constraint (16), and the mean error computed according to Eq. (6).

global integrability conditions leads to more accurate geodesic distance, but the improvement is minor. In fact, in all our experiments, the original formulation already produces results that are close to the exact geodesic distance even for surfaces of complex topology, leaving little room of improvement. Although without a formal proof, we believe this is because the unit vector fields derived from heat diffusion are already close to the gradients of exact geodesic distance [Crane et al. 2013]. As a result, in practice the simple compatibility condition (9) is often enough to prevent pathological cases such as the cylinder example. Therefore, unless stated otherwise, all our results are generated using only constraint (9) to enforce integrability.

### 4.2 Multiple sources

Our method can be easily extended to the case of multiple sources. Following [Crane et al. 2013], we compute an initial unit vector field via heat diffusion from a generalized Dirac over the source set. This leads to a linear system with the same matrix as (3) and a different right-hand-side. Our solver for single-source heat diffusion can be easily adapted to solve this linear system: we construct the breadth-first vertex sets  $\{\mathcal{D}_i\}$  by including all source vertices into  $\mathcal{D}_0$  and collecting  $\mathcal{D}_j$  ( $j \geq 1$ ) according to the same definitions as in Eq. (4); then the Gauss-Seidel iteration proceeds exactly the same as Section 3.1. Afterwards, we find the closest integrable gradient field  $\{\mathbf{g}_i\}$  and integrate it to recover the geodesic distance, in the same way as Sections 3.2 and 3.3. Strictly speaking, when computing a  $\{\mathbf{g}_i\}$  we need to enforce an additional constraint: since all source vertices have the same geodesic distance, the line integral of  $\{\mathbf{g}_i\}$  along any path connecting two source vertices must vanish. This can be enforced by finding a shortest edge path  $S$  from one source to each of the other sources, and introducing a constraint

$$\sum_{e_j \in S} \mathbf{e}_j \cdot \mathbf{g}_{e_j} = 0, \quad (17)$$

where  $e_j$  is an edge on the path,  $\mathbf{e}_j$  is its vector in the same orientation as the path, and  $\mathbf{g}_{e_j}$  is the gradient variable on a face adjacent to  $e_j$ . The modified formulation is still convex and can be solved using ADMM. In our experiments, however, the original formulation already produces results that are close enough to the exact solution, and the additional constraint (17) makes only limited improvement (see Fig. 6 for example). Again, this is likely due to the fact that

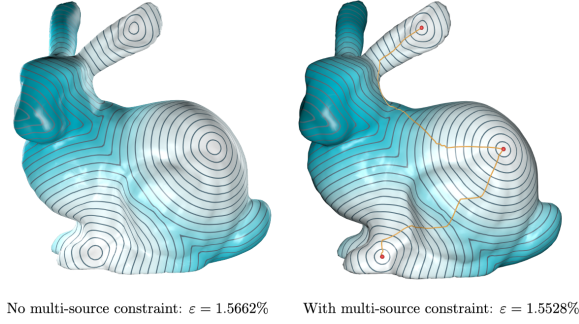


Fig. 6. Multi-source geodesic distance on the bunny surface, computed with and without the constraint (17), and the mean error computed according to Eq. (6).

the unit vector field derived from heat diffusion is already close to the gradients of exact geodesic distance. Moreover, our method for recovering geodesic distance from  $\{g_i\}$  always sets the distance at source vertices to zero, which ensures correct values at the sources even if the computed gradient field violates the constraint (17).

## 5 EXPERIMENTAL RESULTS & DISCUSSIONS

We implemented our algorithm in C++ and used OpenMP for parallelization. we set the heat diffusion time  $t = mh^2$ , where  $h$  is the average edge length and  $m$  is the smooth factor. We search the smooth factor to minimize the mean error relative to the VTP method [Qin et al. 2016] for all the test examples in Tab. 1. Setting the maximal iteration of the ADMM solver  $i_{max} = 10$ , we observe a good balance between speed and accuracy (see Figure ??).

In the following, we evaluate the performance of our algorithm, and compare it with the state-of-the-art methods, including the original heat method (HM) with Cholesky decomposition, the variational heat method (Variational-HM) [Belyaev and Fayolle 2015], and the VTP method. All examples were run on a desktop PC with an Intel Core i7 octa-core CPU at 3.6GHz and 128GB of RAM. Tab. 1 reports the running time, peak memory consumption, and accuracy of various methods. For the original heat method, we show its pre-computation time for Laplacian matrix factorization and the solving time for back substitution separately. For our method, we show the computational time using eight threads. VTP computes the exact discrete geodesic distances, which are used as the baseline to measure accuracy of the approximate methods. We report the mean relative error in Tab. 1. The mean relative error is defined as

$$\text{mean relative error} = \frac{1}{n} \sum \frac{|x_{\text{true}} - x_{\text{test}}|}{|x_{\text{true}}|},$$

where the  $n$  test samples include all the vertices except for the sources. For a fair comparison, for both HM and Variational-HM the linear system matrix factorization is done using the MA87 routine from the HSL library [HSL 2018], which is a multicore sparse Cholesky factorization method [Hogg et al. 2010].

**Space and Time Complexity.** Fig. 7 compares the growth rates of the computational time and memory footprint between different methods using meshes with the same underlying geometry in different resolutions. The graphs verify the  $O(n^2)$  time complexity of

VTP as well as the fast growth of memory footprint for the original heat method, which cause scalability issues for both methods. In comparison, our method achieves near linear growth in both computational time and peak memory consumption, allowing it to handle much larger meshes. In particular, on a high-end workstation with 128GB memory, our method can process meshes with up to 99M vertices (see Table 1).

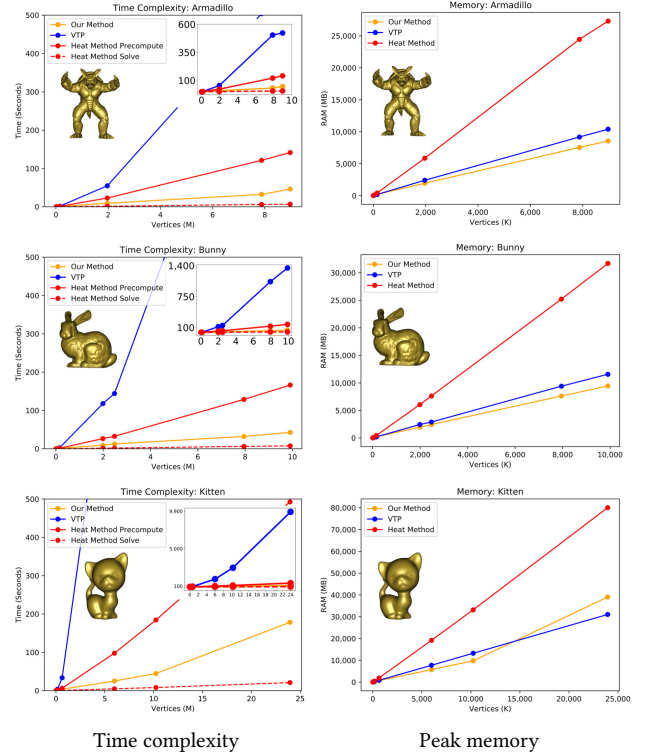


Fig. 7. Time and memory consumption.

**Parallelization.** To evaluate the speedup of the parallel version, we re-run our program on the same model using one, two, four and eight threads, respectively. We fix the Gauss-Seidel iteration count to 600 in the experiments. Fig. 8 shows the timing and the percentage of different steps within the total time. We observe that the ratio of the running time for each step is roughly the same with different numbers of threads, and the total computational is almost inversely proportional to the number of threads. This indicates a high level of parallelism and low overhead of our method, which scales well with the number of processors.

**Comparison with the conjugate gradient method.** In our method, we adopt the Gauss-Seidel solver to diffuse heat and the ADMM solver to recover the geodesic distance. It is worth noting that the conjugate gradient (CG) method is also a popular approach for solving sparse linear system (Poisson equations in this case) due to its memory efficiency. As the Poisson system is only positive semi-definite, we choose the bi-conjugate gradient stabilized method as the Krylov subspace solver for both heat diffusion and distance recovery. We compare our GS+ADMM solver with the CG solver

Table 1. Statistics. We compare our method with VTP, the fast marching method and the heat method.  $n$  is the number of vertices,  $\epsilon$  is the mean error, and RAM (MB) is the peak memory. For the heat method, we adopt a divide-and-conquer method to search the optimal smooth factor  $m$  for a near optimal mean error. For our method, we fix the number of ADMM iterations to 10 and adjust the Gauss-Seidel iterations by step of 100 until the mean error is approximate 1%. Time was measured in seconds on a PC with an 8-core CPU and 128 GB memory.

Model ( $n$ )	VTP		HM					Variational-HM					Ours			
	Time	RAM	Precompute	Solve	RAM	$\epsilon$	$m$	Precompute	Solve	RAM	$\epsilon$	$m$	Time	RAM	$\epsilon$	GS Iters
Triomphe ( 997,635 )	17.66	1,218	10.22	0.69	2,951	0.31%	1.0	11.70	5.55	3,265	0.44%	1.0	2.78	1,071	0.79%	200
Connector ( 2,002,322 )	224.82	2,502	26.17	1.54	6,160	0.15%	2.3	29.34	11.69	6,805	0.14%	2.3	7.01	1,974	0.83%	400
Chineselion ( 3,979,442 )	235.78	4,849	54.69	3.07	12,207	0.73%	3.1	61.31	23.78	13,426	0.52%	3.4	12.89	3,828	0.96%	400
Tricep ( 7,744,320 )	178.41	9,664	115.97	5.71	23,945	0.84%	12.6	129.07	48.61	26,377	0.59%	13.4	34.64	7,417	1.09%	600
Welshdragon ( 9,884,764 )	568.54	12,394	153.34	7.24	30,677	1.21%	11.1	171.24	63.67	33,720	0.91%	11.8	43.69	9,420	1.02%	700
Lucy ( 16,092,674 )	1320.15	18,670	281.97	12.69	51,144	0.46%	13.0	310.01	113.99	56,186	0.29%	13.9	81.88	15,370	1.01%	700
HappyGargoyle ( 19,860,482 )	5060.72	23,464	388.87	16.46	65,545	0.29%	15.7	424.81	149.45	71,644	0.21%	16.6	98.90	18,957	1.06%	1000
Cyvasse ( 39,920,642 )	12363.21	46,976	Out of Memory					Out of Memory					324.08	38,027	1.00%	1800
TwoHeadedBunny ( 40,103,938 )	16681.46	47,258	Out of Memory					Out of Memory					301.71	38,202	0.99%	1700
MalteseFalcon ( 79,899,650 )	28309.32	93,127	Out of Memory					Out of Memory					741.13	76,106	0.99%	1700
Thundercrab ( 98,527,234 )	22298.76	114,610	Out of Memory					Out of Memory					1174.45	93,850	1.24%	2000

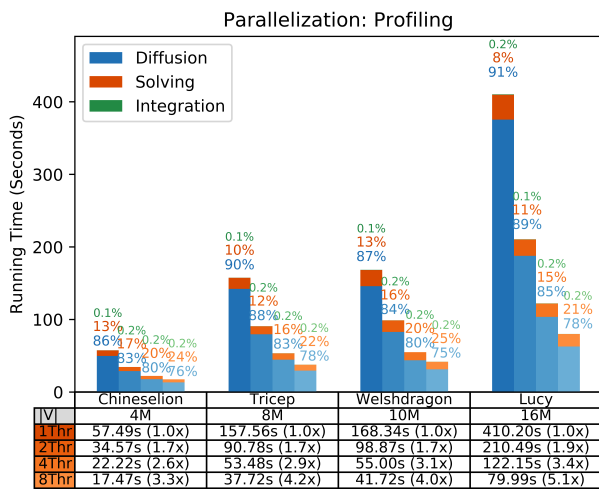


Fig. 8. Profiling. We measure the timing for the 3 steps of our method on 1, 2, 4 and 8 cores, respectively. We observe that the percentages of the 3 steps are nearly consistent, confirming that all steps have linear time complexities. The 3 numbers of each bar are the percentages of the 3 steps: heat diffusion using Gauss-Seidel method (blue), ADMM solver (orange) and gradient integration (green). All the examples are tested with 600 Gauss-Seidel iterations and 10 ADMM iterations.

in terms of time and accuracy. For Gauss-Seidel versus CG, we compute the  $\ell_2$ -norm of the residual as

$$\|(A - tL_c)x - u_0\|^2,$$

in Eq. (3). For ADMM versus CG, we compare the solutions of both methods to the Eigen LDLT solver because ADMM is used for optimization problems and not applicable to the residual. The mean error is represented by

$$\frac{1}{n} \|u - v\|^2,$$

where  $n$  is the element number of ADMM or CG solution vector  $u$  and the Eigen LDLT solution vector  $v$ . As Fig. 9 shows, both Gauss-Seidel and ADMM converge faster than CG.

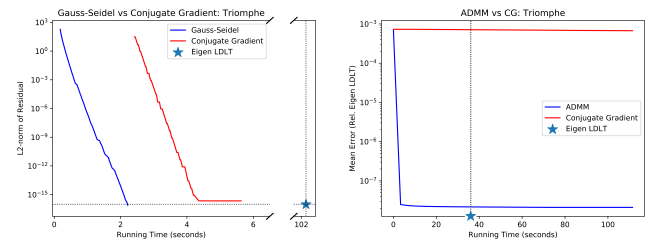


Fig. 9. Comparison of our method with the conjugate gradient method. Our method converges faster than CG.

**Limitations.** Similar to the original heat method, our method is also sensitive to the triangulation quality. The accuracy can be improved using Delaunay triangulation [Liu et al. 2015], but at the cost of increasing mesh complexity.

## 6 CONCLUSION & FUTURE WORK

In this paper, we develop a scalable approach to compute geodesic distance on mesh surfaces. Our method adopts a similar approach as the heat method, first approximating the geodesic distance gradients via heat diffusion, and then recovering the distance by integrated a corrected gradient field. Unlike the heat method which achieves this by solving two linear systems, we propose novel algorithms that can be easily parallelize and with fast convergence. The resulting method significantly outperforms the heat method while producing results with comparable accuracy. Moreover, its memory consumption grows linearly with respect to the mesh size, allowing it to handle much larger models. We perform extensive experiments to evaluate its speed, accuracy, and robustness. The results verify the efficiency and scalability of our method.

Our method can be improved in different aspects. First, although we only implement our method on CPUs using OpenMP, its massive parallelism allows it to be easily ported to GPUs, which we will leave as future work. Second, our algorithm is currently limited to meshes because of its reliance on a well-defined discrete gradient operator. As an extension, we would like to explore its application on other geometric representations such as point clouds and implicit surfaces. Finally, despite experiments showing that our formulation can handle surfaces of non-zero topology as well as multiple sources



by only enforcing local compatibility of the gradients, we do not have a formal proof of this property. An interesting future research is to investigate how the accuracy of heat flow gradients affects the effectiveness of our formulation.

## REFERENCES

- Alexander G. Belyaev and Pierre-Alain Fayolle. 2015. On Variational and PDE-Based Distance Function Approximations. *Computer Graphics Forum* 34, 8 (2015), 104–118.
- Stephen Boyd, Neal Parikh, Eric Chu, Borja Peleato, and Jonathan Eckstein. 2011. Distributed Optimization and Statistical Learning via the Alternating Direction Method of Multipliers. *Found. Trends Mach. Learn.* 3, 1 (2011), 1–122.
- Jindong Chen and Yijie Han. 1990. Shortest Paths on a Polyhedron. In *Proceedings of the Sixth Annual Symposium on Computational Geometry (SCG '90)*. ACM, New York, NY, USA, 360–369.
- Keenan Crane, Mathieu Desbrun, and Peter Schröder. 2010. Trivial Connections on Discrete Surfaces. *Computer Graphics Forum* 29, 5 (2010), 1525–1533.
- Keenan Crane, Clarisse Weischedel, and Max Wardetzky. 2013. Geodesics in heat: A new approach to computing distance based on heat flow. *ACM Trans. Graph.* 32, 5 (2013), 152:1–152:11.
- Keenan Crane, Clarisse Weischedel, and Max Wardetzky. 2017. The Heat Method for Distance Computation. *Commun. ACM* 60, 11 (2017), 90–99.
- David Eppstein. 2003. Dynamic Generators of Topologically Embedded Graphs. In *Proceedings of the Fourteenth Annual ACM-SIAM Symposium on Discrete Algorithms (SODA '03)*. 599–608.
- Anne Greenbaum, Congming Li, and Han Zheng Chao. 1989. Parallelizing preconditioned conjugate gradient algorithms. *Computer Physics Communications* 53, 1 (1989), 295–309.
- Felix Heide, Steven Diamond, Matthias Nießner, Jonathan Ragan-Kelley, Wolfgang Heidrich, and Gordon Wetzstein. 2016. ProxImaL: efficient image optimization using proximal algorithms. *ACM Trans. Graph.* 35, 4 (2016), 84:1–84:15.
- J. D. Hogg, J. K. Reid, and J. A. Scott. 2010. Design of a Multicore Sparse Cholesky Factorization Using DAGs. *SIAM J. Sci. Comput.* 32, 6 (2010), 3627–3649.
- HSL. 2018. A collection of Fortran codes for large scale scientific computation. (2018).
- R. Kimmel and J. A. Sethian. 1998. Computing geodesic paths on manifolds. *Proceedings of the National Academy of Sciences* 95, 15 (1998), 8431–8435.
- Yong-Jin Liu, Chunxu Xu, Dian Fan, and Ying He. 2015. Efficient construction and simplification of Delaunay meshes. *ACM Trans. Graph.* 34, 6 (2015), 174:1–174:13.
- Joseph S.B. Mitchell, David M. Mount, and Christos H. Papadimitriou. 1987. The discrete geodesic problem. *SIAM J. Comput.* 16, 4 (1987), 647–668.
- Michael K. Ng, Pierre Weiss, and Xiaoming Yuan. 2010. Solving Constrained Total-variation Image Restoration and Reconstruction Problems via Alternating Direction Methods. *SIAM J. Scientific Computing* 32, 5 (2010), 2710–2736.
- M. Overby, G. E. Brown, J. Li, and R. Narain. 2017. ADMM $\supseteq$ Projective Dynamics: Fast Simulation of Hyperelastic Models with Dynamic Constraints. *IEEE Transactions on Visualization and Computer Graphics* 23, 10 (2017), 2222–2234.
- Yipeng Qin, Xiaoguang Han, Hongchuan Yu, Yizhou Yu, and Jianjun Zhang. 2016. Fast and Exact Discrete Geodesic Computation Based on Triangle-oriented Wavefront Propagation. *ACM Trans. Graph.* 35, 4 (2016), 125:1–125:13.
- Vitaly Surazhsky, Tatiana Surazhsky, Danil Kirsanov, Steven J. Gortler, and Hugues Hoppe. 2005. Fast Exact and Approximate Geodesics on Meshes. *ACM Trans. Graph.* 24, 3 (2005), 553–560.
- S.R.S. Varadhan. 1967. On the behavior of the fundamental solution of the heat equation with variable coefficients. *Communications on Pure and Applied Mathematics* 20, 2 (1967), 431–455.
- Yilun Wang, Junfeng Yang, Wotao Yin, and Yin Zhang. 2008. A New Alternating Minimization Algorithm for Total Variation Image Reconstruction. *SIAM J. Imaging Sciences* 1, 3 (2008), 248–272.
- Ofir Weber, Yohai S. Devir, Alexander M. Bronstein, Michael M. Bronstein, and Ron Kimmel. 2008. Parallel Algorithms for Approximation of Distance Maps on Parametric Surfaces. *ACM Trans. Graph.* 27, 4 (2008), 104:1–104:16.
- Shi-Qing Xin and Guo-Jin Wang. 2009. Improving Chen and Han's Algorithm on the Discrete Geodesic Problem. *ACM Trans. Graph.* 28, 4 (2009), 104:1–104:8.
- Li Xu, Cewu Lu, Yi Xu, and Jiaya Jia. 2011. Image smoothing via  $L_0$  gradient minimization. *ACM Trans. Graph.* 30, 6 (2011), 174:1–174:12.
- Xiang Ying, Xiaoning Wang, and Ying He. 2013. Saddle vertex graph (SVG): A novel solution to the discrete geodesic problem. *ACM Transactions on Graphics* 32, 6 (2013), 170:1–12.
- Xiang Ying, Shi-Qing Xin, and Ying He. 2014. Parallel Chen-Han (PCH) Algorithm for Discrete Geodesics. *ACM Transactions on Graphics* 33, 1 (2014), 9:1–9:11.